JPhys Photonics

PAPER • OPEN ACCESS

Lateral resolution enhanced interference microscopy using virtual annular apertures

To cite this article: Peter Lehmann *et al* 2023 *J. Phys. Photonics* **5** 015001

View the article online for updates and enhancements.

You may also like

- Low coherent Linnik interferometer optimized for use in nano-measuring machines
Jan Niehues, Peter Lehmann and Weichang Xie
- Identification of damage parameters of a full-scale steel structure damaged by seismic loading
Edgar Görl and Michael Link
- Optical MEMS-based micromirror arrays for active light steering in smart windows
Hartmut Hillmer, Basim Al-Qargholi, Muhammad Mohsin Khan et al.

Journal of Physics: Photonics

OPEN ACCESS

RECEIVED
21 October 2022

REVISED
8 January 2023

ACCEPTED FOR PUBLICATION
11 January 2023

PUBLISHED
27 January 2023

Original Content from this work may be used under the terms of the Creative Commons Attribution 4.0 licence.

Any further distribution of this work must maintain attribution to the author(s) and the title of the work, journal citation and DOI.

PAPER

Lateral resolution enhanced interference microscopy using virtual annular apertures

Peter Lehmann[1,3,*], Lucie Hüser[1], Andre Stelter[1] and Thomas Kusserow[2,3]

[1] Measurement Technology Group, Faculty of Electrical Engineering and Computer Science, University of Kassel, Wilhelmshoeher Allee 71, 34121 Kassel, Germany
[2] Institute of Nanostructure Technologies and Analytics (INA), University of Kassel, Heinrich-Plett-Straße 40, 34132 Kassel, Germany
[3] Center for Interdisciplinary Nanostructure Science and Technology (CINSaT), University of Kassel, Heinrich-Plett-Straße 40, 34132 Kassel, Germany
[*] Author to whom any correspondence should be addressed.

E-mail: p.lehmann@uni-kassel.de

Keywords: interference microscopy, coherence scanning interferometry, three-dimensional transfer function, lateral resolution, Fourier optics, Kirchhoff approximation

Abstract

The lateral resolution in microscopic imaging generally depends on both, the wavelength of light and the numerical aperture of the microscope objective lens. To quantify the lateral resolution Ernst Abbe considered an optical grating illuminated by plane waves. In contrast, the Rayleigh criterion holds for two point sources or point scatterers separated by a lateral distance, which are supposed to emit spherical waves. A portion of each spherical wave is collected by the objective lens and results in an Airy disc corresponding to a diffraction limited intensity point spread function (PSF). If incoherent illumination is employed the intensity PSFs related to different scatterers on an object are added resulting in the well-known Rayleigh resolution criterion. In interference microscopy instead of the intensity the electric field scattered or diffracted by an object will be affected by the transfer function of the optical imaging system. For a reflective object the lateral resolution of an interference microscope can be again characterized by the Abbe limit if the object under investigation is a grating. However, if two irregularities on a flat surface are being imaged the resolution no longer obeys the Rayleigh criterion. Instead, it corresponds to an optical system with an annular aperture and thus surpasses the prediction given by the Rayleigh criterion. This holds true for both, amplitude as well as phase objects, as it will be elucidated in this study by theoretical considerations, simulation results and an experimental proof of principle.

1. Introduction

Extending the lateral resolution capabilities of optical microscopes is an essential subject of current research as it directly enables the investigation of structure dimensions below the diffraction limit and thus broadens the range of application of microscopic two- and three-dimensional imaging. Various resolution enhancement and super-resolution techniques have been investigated in context with conventional and confocal optical microscopy with particular focus on biological objects [1, 2]. These methods are mostly dedicated to fluorescence microscopy and thus require a special labelling of the specimen under investigation. Since we are primary interested in characterizing nanostructured surfaces produced by engineering processes, fluorescence methods are not subject of this contribution as labelling is not desired in this context. Label-free methods for resolution enhancement are based on structured illumination microscopy [3] and microsphere assisted microscopy [4], for example. In contrast, in interference microscopy resolution enhancement techniques are rarely applied till now. Nevertheless, techniques such as microsphere-assistance or immersion systems known from conventional microscopic imaging are being used in interference microscopy too [4–9].

© 2023 The Author(s). Published by IOP Publishing Ltd

However, due to the complex composition of signals additional options for resolution enhancement exist in interference microscopy. For example, it is well known that improved lateral resolution can be achieved by use of annular apertures located in both, the illumination pupil as well as the pupil plane of the imaging path of a microscope [10–12]. If reflective phase objects or three-dimensional micro-topographies are to be measured, interference microscopy is often employed in order to gain depth information [13]. A so-called depth scan changes the distance between the microscope and the object and thus, recording a series of images results in a 3D image stack, which enables the numerical reconstruction of the surface topography. As a consequence, the transfer characteristics of a depth scanning microscope can be best described by an optical 3D transfer function [14–21]. The two lateral spatial frequency coordinates of the 3D transfer function are related to the transversal spatial frequency axes of the microscopic image. The axial spatial frequency results from the interference signals occurring due to the depth scan. A familiar approach in this context is to define a so-called equivalent wavelength of the interferogram and to use conventional two-dimensional Fourier optics modeling [22]. However, we recently derived an analytic expression for the 3D transfer function of an interference microscope that holds for surface topographies characterized by specular reflection and diffraction [20, 21]. It should be noted that the spectral composition of an interference signal depends not only on the spectral distribution of the light source and the spectral sensitivity of the camera but also on the pupil functions of the microscope and the predominant lateral spatial frequencies of the surface topography [23, 24]. If, for simplicity, monochromatic light is used, the pupil function and the lateral spatial frequency distribution of the object's surface will be most dominant. Here, we presume constant intensity in the illuminating pupil plane and a constant apodization factor due to specular reflection, what leads to an unambiguous 3D transfer function [21]. Therefore, the lateral spatial frequency distribution of an interference image stack is given by the 3D spatial frequency representation of the complex reflection function of the measuring object. This spatial frequency distribution is weighted by the 3D transfer function. On the other hand, the axial spatial frequency corresponds to the frequency, for which an interference signal of a single camera pixel is analyzed and thus can be varied by setting the parameters of the signal processing algorithm. We call the relevant parameter 'evaluation wavelength'. This is the wavelength, which is used to calculate the phase value and the envelope position of a CSI (coherence scanning interferometry) measurement signal. With the evaluation wavelength λ_{eval} the corresponding axial spatial frequency value $q_{z,\mathrm{eval}}$ results in:

$$q_{z,\mathrm{eval}} = 4\pi/\lambda_{\mathrm{eval}} \in \left[4\pi\sqrt{1-\mathrm{NA}^2}/\lambda_0\,,\,4\pi/\lambda_0\right], \tag{1}$$

i.e.

$$\lambda_{\mathrm{eval}} \in \left[\lambda_0,\,\lambda_0\Big/\sqrt{1-\mathrm{NA}^2}\right], \tag{2}$$

where λ_0 is the central wavelength of light, emitted by the light source and NA represents the numerical aperture of the system. In the following we will show that the 2D transfer function in the $q_x q_y$-plane corresponding to a certain choice of λ_{eval} shows significant changes along the q_z-axis. This is accompanied by a strong dependence of the lateral resolution capabilities on the evaluation wavelength. We demonstrate that the highest lateral resolution is reached for the maximum evaluation wavelength $\lambda_{\mathrm{eval}} = \lambda_0\Big/\sqrt{1-\mathrm{NA}^2}$. For a grating the achievable lateral resolution δ_A corresponds to the diffraction limited resolution given by the Abbe limit $\delta_A = 0.5\,\lambda/\mathrm{NA}$. Lateral resolution beyond the fundamental Abbe limit is sometimes referred to as super-resolution [25]. However, with respect to the smallest resolvable distance between two irregularities in microscopic imaging with incoherent illumination the Rayleigh resolution criterion $\delta_R = 0.61\,\lambda/\mathrm{NA}$ becomes relevant [25]. In the following sections we show that lateral resolution well below the value given by the Rayleigh criterion can be reached employing interference microscopy and using what we call a virtual annular aperture.

The experimental setup used throughout this study is shown schematically in figure 1(a). An interference signal called correlogram is obtained during the depth-scan along the z-axis from a flat area of polished silicon. Figure 1(b) displays a correlogram employing a royal blue LED of 447 nm central wavelength and 20 nm wavelength bandwidth (FWHM) for illumination. The low number of visible interference fringes is due to the high NA of 0.9 of the objective lenses. The absolute value of the Fourier transformed correlogram plotted over the wavelength scale in figure 1(c) demonstrates that the spectrum of the correlogram is much broader than the spectrum of the light source and extends to wavelengths of more than 1000 nm. This phenomenon leads to the well-known NA-effect [26–29], which is usually considered by the equivalent wavelength instead of the central wavelength of the light source in CSI signal processing [22].

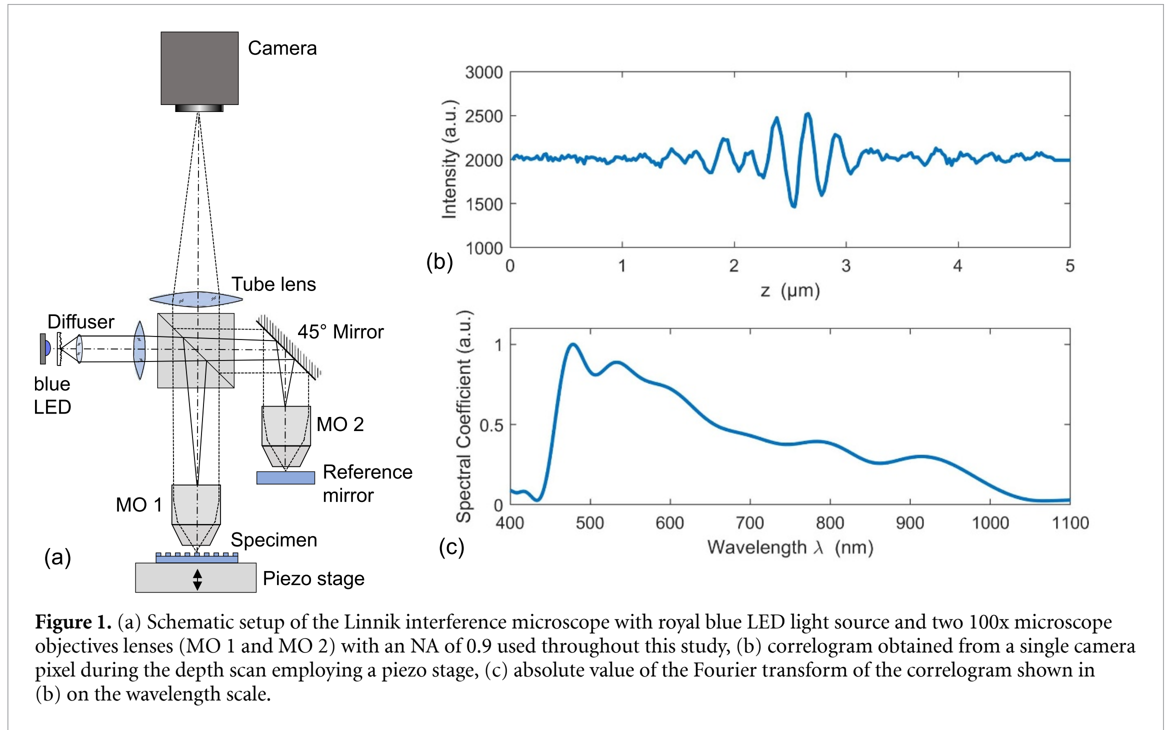

Figure 1. (a) Schematic setup of the Linnik interference microscope with royal blue LED light source and two 100x microscope objectives lenses (MO 1 and MO 2) with an NA of 0.9 used throughout this study, (b) correlogram obtained from a single camera pixel during the depth scan employing a piezo stage, (c) absolute value of the Fourier transform of the correlogram shown in (b) on the wavelength scale.

2. Three-dimensional transfer function

As mentioned above, three-dimensional transfer functions (3D TFs) represent the full transfer capabilities of microscope systems in the spatial frequency domain. 3D TFs can be obtained from the Ewald sphere representation of the wave vectors of incident plane waves and waves scattered from a point object [10]. The limitation of the angular distribution of these wave vectors by the numerical aperture of a microscope objective lens results in truncated spherical caps instead of full spheres as it was pointed out by McCutchen [30]. Thus, the corresponding Ewald spheres are sometimes called McCutchen spheres [18]. The 3D TF of a microscope results from a three-dimensional correlation of the spherical caps corresponding to the incident and scattered wave vectors [16, 20]. According to our previous studies mentioned above, the shape of the 3D TF of a diffraction limited interference microscope with uniform monochromatic pupil illumination of wavelength λ_0 depends on the surface under investigation [20, 21]. In contrast to surfaces characterized by single point scatterers for specularly reflective or diffractive continuous surfaces the normalized 3D TF results in:

$$\begin{aligned} &H(q_\rho, q_z, k_0) = \frac{q_z}{2k_0} \quad \text{for} \quad q_{z,0} \leqslant q_z \leqslant q_{z,\max}, \\ &H(q_\rho, q_z, k_0) = \left(1 - \frac{2}{\pi}\arccos\left(\frac{|\mathbf{q}|\,(q_z - q_{z,\min})}{q_\rho\sqrt{4k_0^2 - |\mathbf{q}|^2}}\right)\right)\frac{q_z}{2k_0} \\ &\qquad \text{for} \quad q_{z,\min} \leqslant q_z < q_{z,0}, \\ &H(q_\rho, q_z, k_0) = 0 \qquad \text{elsewhere}. \end{aligned} \tag{3}$$

The vector $\mathbf{q}$ in the spatial frequency domain with transverse spatial frequency $q_\rho = \sqrt{q_x^2 + q_y^2}$ and axial spatial frequency q_z represents the difference between the wave vector $\mathbf{k}_s$ of the scattered light field and the wave vector $\mathbf{k}_{in}$ of the incident wave:

$$\mathbf{q} = \mathbf{k}_s - \mathbf{k}_{in} = k_0 \begin{pmatrix} \sin(\theta_s)\cos(\phi_s) - \sin(\theta_{in})\cos(\phi_{in}) \\ \sin(\theta_s)\sin(\phi_s) - \sin(\theta_{in})\sin(\phi_{in}) \\ \cos(\theta_{in}) + \cos(\theta_s) \end{pmatrix}. \tag{4}$$

$\mathbf{q}$ is defined in terms of the wavenumber $k_0 = 2\pi/\lambda_0$ and the polar and azimuth angles θ_{in} and ϕ_{in} of the incident wave as well as the angles θ_s and ϕ_s of the scattered wave. Considering the distance q_ρ from the q_z axis of a system with the numerical aperture NA, the values $q_{z,\min}$, $q_{z,0}$ and $q_{z,\max}$ are given by:

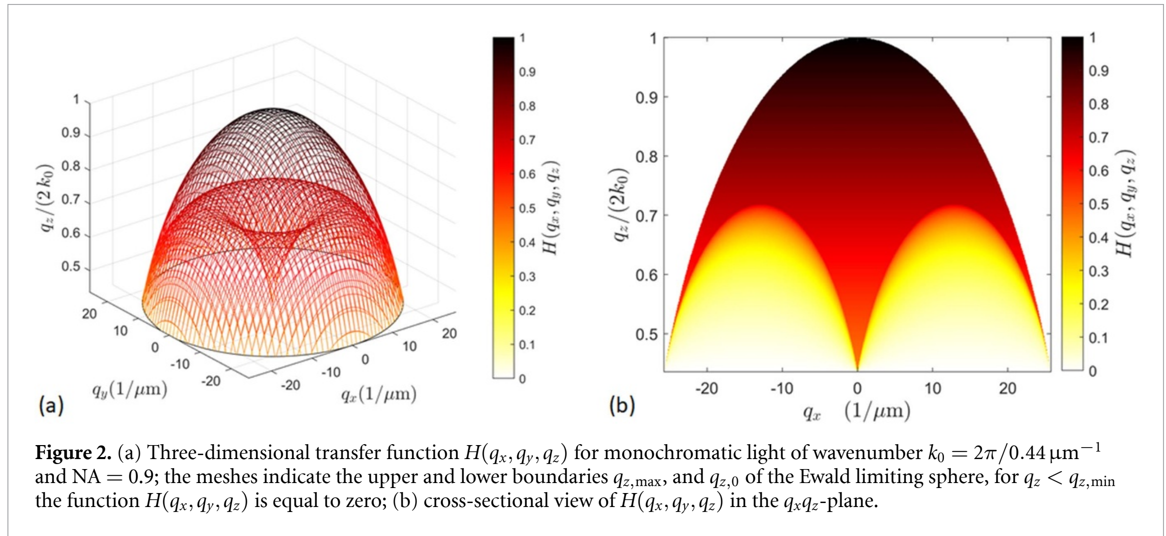

Figure 2. (a) Three-dimensional transfer function $H(q_x, q_y, q_z)$ for monochromatic light of wavenumber $k_0 = 2\pi/0.44\,\mu\text{m}^{-1}$ and NA = 0.9; the meshes indicate the upper and lower boundaries $q_{z,\max}$, and $q_{z,0}$ of the Ewald limiting sphere, for $q_z < q_{z,\min}$ the function $H(q_x, q_y, q_z)$ is equal to zero; (b) cross-sectional view of $H(q_x, q_y, q_z)$ in the q_xq_z-plane.

$$
\begin{aligned}
q_{z,\min} &= 2k_0\sqrt{1-\mathrm{NA}^2},\\
q_{z,0} &= k_0\sqrt{1-\mathrm{NA}^2} + k_0\sqrt{1-(q_\rho/k_0-\mathrm{NA})^2},\\
q_{z,\max} &= 2k_0\sqrt{1-q_\rho^2/(4k_0^2)}.
\end{aligned}
\tag{5}
$$

For $q_z > q_{z,\max}$ and $q_z < q_{z,\min}$ the 3D TF will cut off, i.e. there will be no more contribution to interference signals. Note that $q_{z,0}$ and $q_{z,\max}$ depend on the transverse spatial frequency q_ρ. The 3D transfer function $H(q_\rho, q_z, k_0) = H(q_x, q_y, q_z)$ for monochromatic light of wavelength $\lambda_0 = 440$ nm and NA = 0.9 is plotted in figure 2(a). The upper and lower meshes are related to the boundaries of $H(q_x, q_y, q_z)$ at $q_{z,\max}$ and $q_{z,0}$. The values of $q_{z,\max}$ represent the outer sphere in figure 2(a), which corresponds to the backscattering directions. The lower mesh is given by $q_{z,0}$ values belonging to the maximum angle of incidence $\theta_{\max}$ with respect to the optical axis. Finally the constant value $q_{z,\min}$ represents the plane, were both, the angle of incidence and the scattering angle, equal $\theta_{\max}$. The colors of the mesh correspond to the values of the function $H(q_x, q_y, q_z)$. Figure 2(b) demonstrates that even for out-of-plane rays related to $q_{z,\min} < q_z < q_{z,0}$, $H(q_x, q_y, q_z)$ shows non-zero values. For $q_x = q_y = 0$, in agreement with [29, 31] $H(q_x, q_y, q_z) = H(q_z)$ is proportional to the axial spatial frequency q_z. Since CSI signals are typically analyzed at a certain evaluation wavelength corresponding to a certain value of q_z, figure 3 shows exemplarily four horizontal 2D cross sections of $H(q_x, q_y)$ at $q_z/2k_0 = 0.77, 0.67, 0.56$, and 0.44. These cross sections are named 'partial transfer function $H_p(q_x, q_y)$' in the following. The radius of the outer circular boundary of a partial transfer function represents the spatial frequency bandwidth of the interference microscope for this particular partial transfer function. The partial transfer functions shown in figure 3 correspond to evaluation wavelengths λ_{eval} of 574, 658, 787, and 1004 nm, respectively. Their shape depending on the lateral spatial frequency q_ρ determines details of the transfer characteristics.

Obviously, the lateral spatial frequency bandwidth, which corresponds to the radius of a given partial TF, increases as the evaluation wavelength increases. In CSI measurement the evaluation wavelength is typically adjusted such that it coincides with the central peak of the spectrum obtained from an interference signal [22, 29]. This corresponds to the partial TF according to figure 3(a), where the evaluation wavelength $\lambda_{\text{eval}} = 574$ nm is approximately 30% longer than the central wavelength $\lambda_0 = 440$ of the illuminating light. Hence, if we select a short evaluation wavelength, i.e. $q_z > q_{z,0}$ the corresponding partial transfer function will be a circular disc (see figure 3(a)) and its Fourier transform leads to an Airy disc in object space as it was found by Abdulhalim [32, 33].

In contrast, the highest lateral resolution is reached for the longest evaluation wavelength $\lambda_{\text{eval}} = 1004$ nm, which corresponds to $q_z/2k_0 = q_{z,\min}/2k_0 = 0.44$. Note that according to figure 3(d) the shape of this partial transfer function equals the partial transfer function for incident and scattered rays including a maximum angle $\theta_{\max}$ with respect to the optical axis. Thus, a similar result is to be expected for an annular aperture of maximum diameter $k_0\,\mathrm{NA}$. However, in case of interference microscopy the evaluation wavelength λ_{eval} can be adjusted by software settings such that no physical annular aperture is necessary. Therefore, we use the term 'virtual annular aperture' in context with long evaluation wavelengths, where light rays contributing to the interference signal propagate under angles $\theta_{\text{in}} \approx \theta_s \approx \theta_{\max}$ with respect to the optical axis.

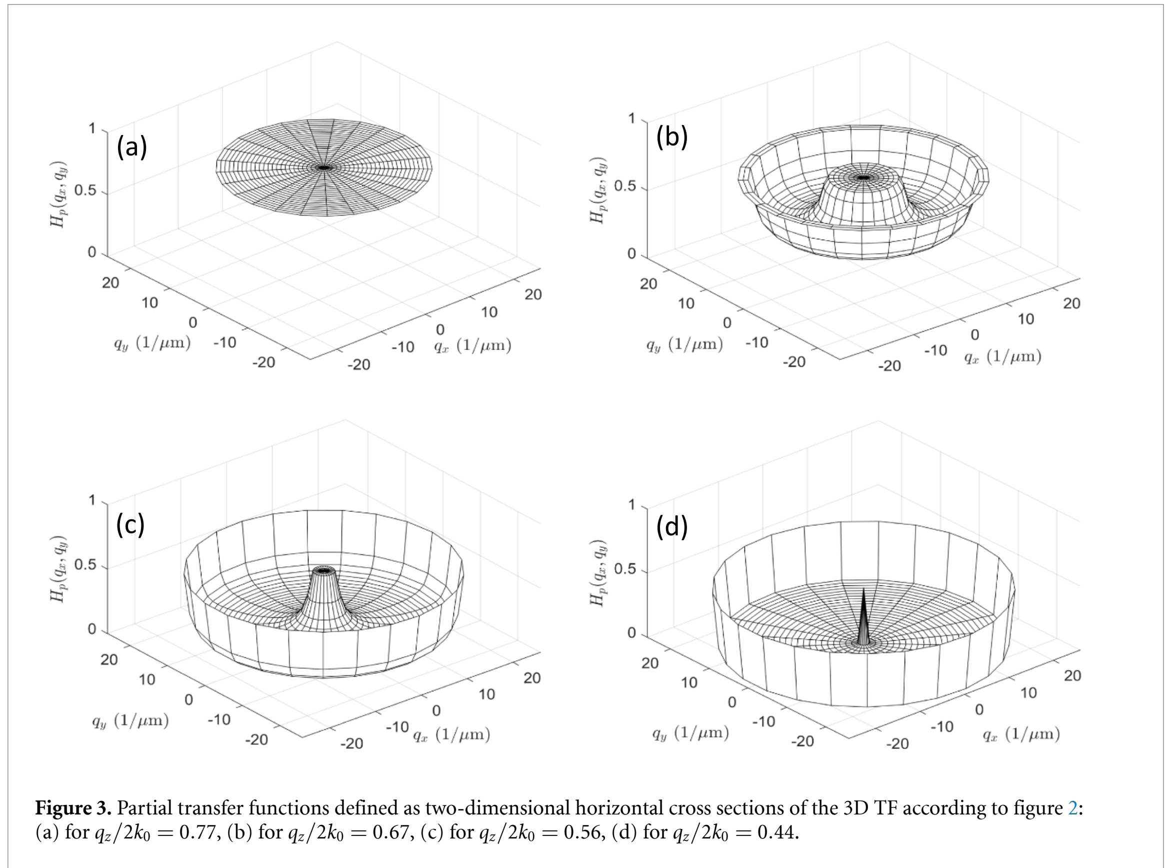

Figure 3. Partial transfer functions defined as two-dimensional horizontal cross sections of the 3D TF according to figure 2: (a) for $q_z/2k_0 = 0.77$, (b) for $q_z/2k_0 = 0.67$, (c) for $q_z/2k_0 = 0.56$, (d) for $q_z/2k_0 = 0.44$.

In order to create a virtual CSI instrument the partial transfer function needs to be multiplied by the scattered light field in the spatial frequency domain. Based on the scalar Kirchhoff or physical optics approximation the scattered light field $U_s(\mathbf{q})$ can be obtained from the field $U_{obj}(x, y, q_z)$ directly above the surface of an object [22, 34, 35]:

$$U_s(\mathbf{q}) = \frac{1}{A}\int_A U_{obj}(x, y, q_z)\,\mathrm{e}^{-\mathrm{i}\left(q_x x + q_y y\right)}\,\mathrm{d}x\,\mathrm{d}y, \tag{6}$$

where the area A of integration corresponds to the field of view of the microscope. Defining an appropriate field illumination function $A(x, y)$ equation (6) can be written as a two-dimensional Fourier transform:

$$U_s(\mathbf{q}) = \frac{1}{A}\int_{-\infty}^{+\infty}\int_{-\infty}^{+\infty} A(x, y)\,U_{obj}(x, y, q_z)\,\mathrm{e}^{-\mathrm{i}\left(q_x x + q_y y\right)}\,\mathrm{d}x\,\mathrm{d}y. \tag{7}$$

Note, that U_{obj} depends on the lateral coordinates x and y and on the axial spatial frequency q_z. This is due to the fact, that in interference microscopy the object is often considered as a pure phase object such that $U_{obj}(x, y, q_z)$ results in:

$$U_{obj}(x, y, q_z) = U_0\,\mathrm{e}^{-\mathrm{i}q_z s(x,y)}, \tag{8}$$

where U_0 is a constant field amplitude and $s(x, y)$ is the surface height function, which modulates the phase of the reflected field directly above the object. The same object field results via Fourier transform with respect to the z coordinate from the so-called foil-model of a surface [21, 36]. However, a reflective object may also cause a spatial amplitude modulation of the field instead of a phase modulation. If the angular dependence of the reflectivity is neglected this results in:

$$U_{obj}(x, y, q_z) = U_{obj}(x, y) = U_0\,a(x, y), \tag{9}$$

where $a(x, y)$ is the amplitude modulation function. Now, in $\mathbf{q}$-space the intensity change $\Delta I(\mathbf{q})$ due to interference, which is transferred by the measuring instrument, results from frequency domain filtering of the Fourier representation of the light field $U_s(\mathbf{q})$ scattered from the object using the 3D transfer function:

$$\Delta I(\mathbf{q}) \sim U_s(\mathbf{q})\,H(\mathbf{q}). \tag{10}$$

However, as mentioned above, in interference microscopy the resulting interferogram is usually analyzed at a certain evaluation wavelength $\lambda_{z,\mathrm{eval}} = 4\pi/q_{z,\mathrm{eval}}$. If this is considered in equation (10) the partial transfer function $H_p(q_x,q_y) = H(q_x,q_y,q_{z,\mathrm{eval}})$ comes into play:

$$\Delta I\left(q_x,q_y\right) \sim U_{\mathrm{s}}\left(q_x,q_y,q_{z,\mathrm{eval}}\right) H_p(q_x,q_y). \tag{11}$$

Consequently, phase and amplitude of the complex interference intensity $\Delta\tilde{I}(x,y)$ in the object space directly follow from inverse 2D Fourier transform of $\Delta I\left(q_x,q_y\right)$:

$$\Delta\tilde{I}(x,y) = \mathcal{F}^{-1}\left\{\Delta I\left(q_x,q_y\right)\right\}. \tag{12}$$

If the object under investigation is a phase object the reconstructed surface height function $s_{\mathrm{rec}}(x,y)$ results from the phase obtained from $\Delta\tilde{I}(x,y)$:

$$s_{\mathrm{rec}}(x,y) = \frac{1}{q_{z,\mathrm{eval}}} \arg\left\{\Delta\tilde{I}(x,y)\right\}. \tag{13}$$

If on the other hand the object is an amplitude object, its reconstructed amplitude distribution $U_0\, a_{\mathrm{rec}}(x,y)$ is given by:

$$U_0\, a_{\mathrm{rec}}(x,y) \sim \mathrm{Re}\{\Delta\tilde{I}(x,y)\}. \tag{14}$$

Note that $U_0\, a_{\mathrm{rec}}(x,y)$ is proportional to the amplitude reflection coefficient and thus may take negative values. In conventional microscopy the intensity distribution $I(x,y)$ of an object can be equivalently obtained as the inverse Fourier transform of the product of the Fourier transformed object intensity $\tilde{I}_{\mathrm{obj}}\left(q_x,q_y\right)$ and the well-known modulation transfer function MTF $\left(q_x,q_y\right)$, which holds for a diffraction limited system with spatially incoherent illumination [37]:

$$I_{\mathrm{rec}}(x,y) = \mathcal{F}^{-1}\left\{\tilde{I}_{\mathrm{obj}}\left(q_x,q_y\right) \mathrm{MTF}\left(q_x,q_y\right)\right\}. \tag{15}$$

Under the assumption of constant pupil illumination the two-dimensional MTF $\left(q_x,q_y\right)$ and the 3D-TF $H(q_x,q_y,q_z)$ are related to each other via the projection slice theorem [38], i.e.:

$$\int_{-\infty}^{+\infty} H(q_x,q_y,q_z)\,\mathrm{d}q_z \sim \mathrm{MTF}\left(q_x,q_y\right). \tag{16}$$

Note that the intensities $I(x,y)$ and $I_{\mathrm{rec}}(x,y)$ are proportional to the reflectivity of intensity and are thus limited to positive values. The MTF $\left(q_x,q_y\right)$ is also used to characterize the 2D transfer characteristics of interference microscopes [22, 39, 40]. However, this approach is just a rough approximation, since in contrast to 2D imaging, interference signals of an image stack are analyzed pixel by pixel with respect to phase and envelope.

In the following we are interested in the question, how good two amplitude or phase irregularities, which are a certain distance apart from each other, can be resolved by interference microscopy. For amplitude objects the results can be compared with the Rayleigh resolution limit, which follows from equation (15).

3. Simulation

In order to elucidate the consequences of the above mentioned transfer characteristics and to point out the differences in lateral resolution between conventional and interference microscopy this section introduces simulation results for both, phase objects as well as amplitude objects. In addition, the discrepancies in lateral resolution in case of gratings of certain period compared to two separated irregularities at a certain lateral distance d from each other will be discussed.

First, we define a test structure, which represents a single irregularity $a_i(x,y)$ of diameter d in the xy-plane:

$$a_i(x,y) = \begin{cases} \pm\frac{1}{2}\left(1+\cos\left(2\pi\sqrt{x^2+y^2}/d\right)\right) & \text{for } \sqrt{x^2+y^2} \leqslant d/2 \\ 0 & \text{else.} \end{cases} \tag{17}$$

This single irregularity can be added periodically to form a 2D amplitude object:

$$a(x,y) = \sum_{m=M_{\min}}^{M_{\max}} \sum_{n=N_{\min}}^{N_{\max}} a_i(x-d/2-m\,d, y-d/2-n\,d). \tag{18}$$

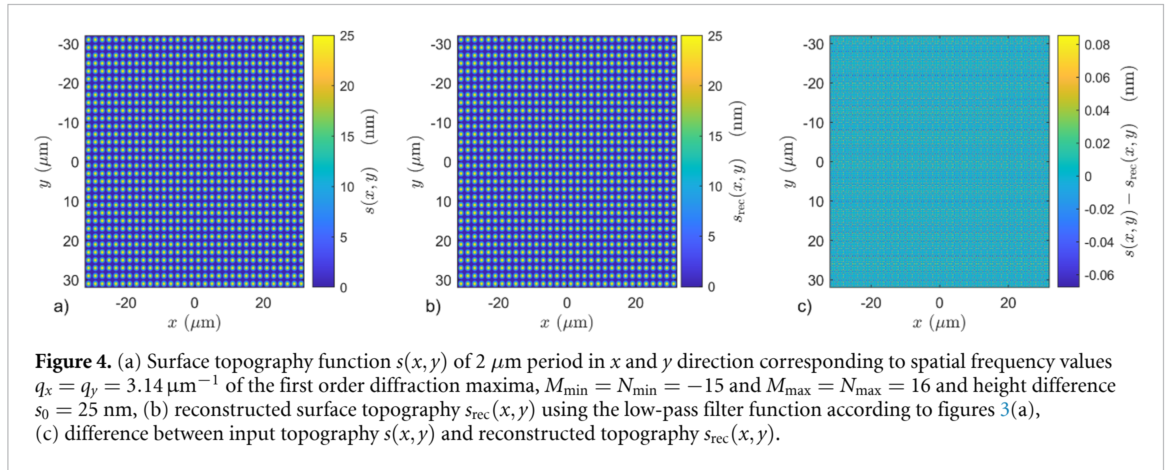

Figure 4. (a) Surface topography function $s(x,y)$ of 2 μm period in x and y direction corresponding to spatial frequency values $q_x = q_y = 3.14\,\mu\text{m}^{-1}$ of the first order diffraction maxima, $M_{\text{min}} = N_{\text{min}} = -15$ and $M_{\text{max}} = N_{\text{max}} = 16$ and height difference $s_0 = 25$ nm, (b) reconstructed surface topography $s_{\text{rec}}(x,y)$ using the low-pass filter function according to figures 3(a), (c) difference between input topography $s(x,y)$ and reconstructed topography $s_{\text{rec}}(x,y)$.

If the difference $M_{\text{max}} - M_{\text{min}}$ is a large number $a(x,y)$ is an amplitude grating in x-direction, and the same for the y-direction. Otherwise, if $M_{\text{min}} = 0$, $M_{\text{max}} = 1$ the object comprises two irregularities in a distance d in x-direction. Using equation (8) and introducing the surface height factor s_0 one can easily transform any amplitude object into a phase object, where:

$$s(x,y) = s_0\, a(x,y), \tag{19}$$

is the surface height function. In the following we assume that the field illumination function $A(x,y)$ extends over an area with dimensions that are very large compared to the distance d between two neighboring surface irregularities. Hence, the periodic extension of $A(x,y)$ due to the application of the discrete Fourier transform does not affect the final result and equation (7) can be seen as a two-dimensional Fourier transform of the object field $U_{\text{obj}}(x,y,q_z)$. Figure 4(a) shows a two-dimensional phase grating corresponding to the surface height function $s(x,y)$ of $d = 2$ μm period and $s_0 = 25$ nm total height difference. Figure 4(b) is the reconstructed surface height function $s_{\text{rec}}(x,y)$, which results if the partial transfer function $H_p(q_x,q_y)$ according to figure 3(a) is used. Figure 4(c) shows the difference between (a) and (b) and indicates a nearly perfect reconstruction, which is due to the rather long period of 2 μm. Note that the reconstructed surface height function shows maximum deviations below 0.1 nm, although the partial transfer function $H_p(q_x,q_y)$ has a constant value of 0.766 over the whole transfer range of:

$$\sqrt{q_x^2 + q_y^2} \leqslant 18.4\,\mu\text{m}^{-1}.$$

This is due to the phase object, where both, the real and the imaginary part are multiplied by the same value, such that the phase angle remains unchanged.

Figure 5(a) shows an amplitude grating $a(x,y)$ with a period d of 170 nm in x and y direction, whereas in figure 5(b) $a(x,y)$ represents an amplitude grating along the x-axis and a double slit in y-direction, i.e. two parallel gratings in x-direction separated by a distance $d = 170$ nm in y-direction. In figure 5(c), $a(x,y)$ shows amplitude irregularities in a quadratic arrangement, i.e. a double slit with $d = 170$ nm in x- and y-direction. Figures 5(d)–(f) represent the absolute values of the 2D Fourier transforms of the input functions $a(x,y)$ according figures 5(a)–(c). After multiplying with the partial transfer function $H_p(q_x,q_y)$ shown in figure 3(d) the reconstructed amplitude reflection functions $a_{\text{rec}}(x,y)$ according to figures 5(g)–(i) result. In this case the maximum transmission spatial frequency is limited by:

$$\sqrt{q_x^2 + q_y^2} \leqslant 25.7\,\mu\text{m}^{-1}.$$

Therefore, the angular grating frequency $2\pi/d = 36.96$ μm^{-1} is blocked by the partial transfer function and in figure 5(g) the grating structure is no longer visible. According to figure 5(e) the Fourier transform of the two parallel gratings of figure 5(b) results in discrete vertical lines representing the diffraction orders of the grating, whereas the double slit arrangement along the y-direction leads to a cosinusoidal modulation along the q_y-axis, which still shows first order contributions different from zero for $|q_y| \leqslant 25.7$ μm^{-1}. Consequently, the vertical double slit structure is resolved in figure 5(h), whereas the grating structure is not. Figure 5(i) shows that the quadratic arrangement of irregularities will be resolved and thus confirms the above argumentation. However, note that the reflectivity changes of the reconstructed amplitude object are much smaller than the original values. This follows from the rather small values of the partial transfer function $H_p(q_x,q_y)$ according to figure 3(d) [20].

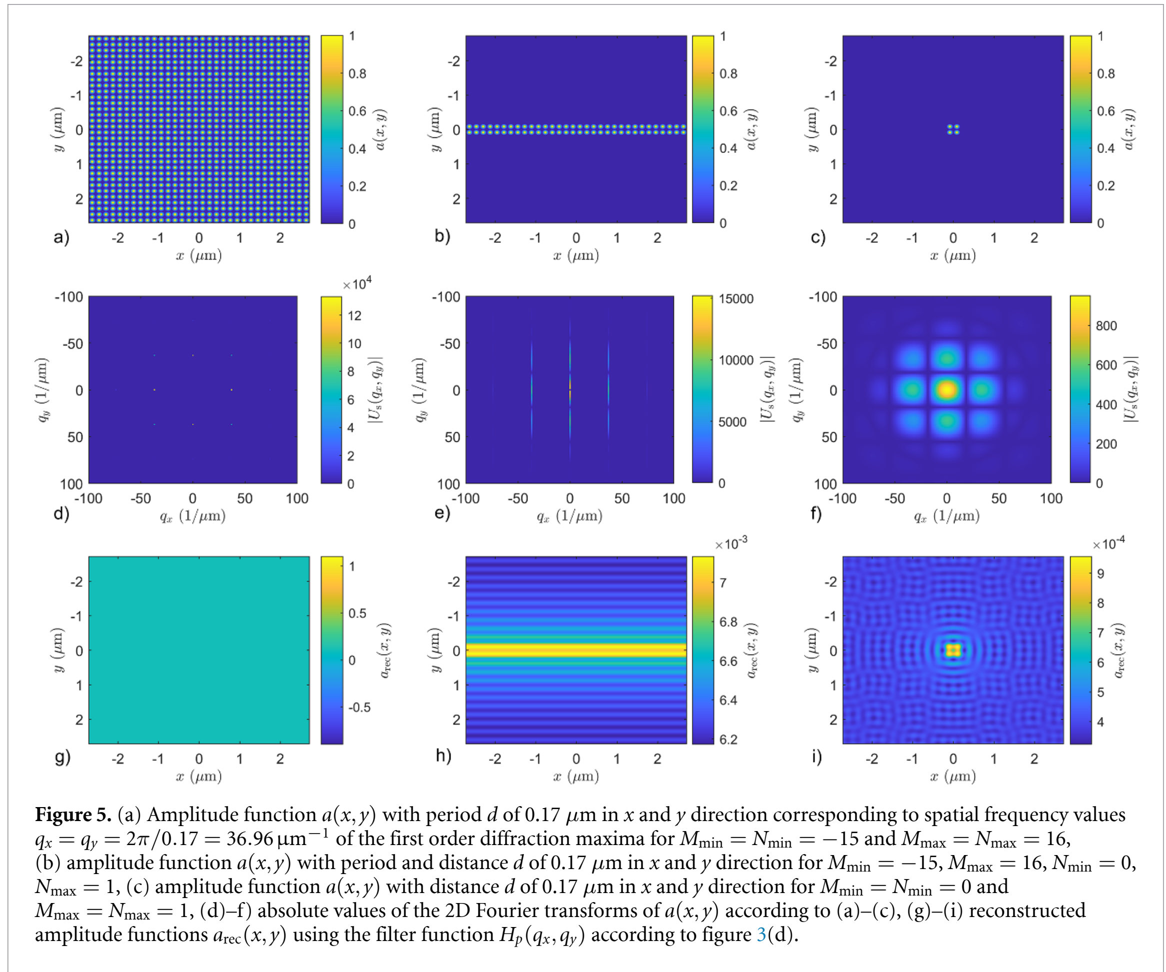

Figure 5. (a) Amplitude function $a(x,y)$ with period d of 0.17 μm in x and y direction corresponding to spatial frequency values $q_x = q_y = 2\pi/0.17 = 36.96\,\mu\text{m}^{-1}$ of the first order diffraction maxima for $M_{\min} = N_{\min} = -15$ and $M_{\max} = N_{\max} = 16$, (b) amplitude function $a(x,y)$ with period and distance d of 0.17 μm in x and y direction for $M_{\min} = -15$, $M_{\max} = 16$, $N_{\min} = 0$, $N_{\max} = 1$, (c) amplitude function $a(x,y)$ with distance d of 0.17 μm in x and y direction for $M_{\min} = N_{\min} = 0$ and $M_{\max} = N_{\max} = 1$, (d)–f) absolute values of the 2D Fourier transforms of $a(x,y)$ according to (a)–(c), (g)–(i) reconstructed amplitude functions $a_{\text{rec}}(x,y)$ using the filter function $H_p(q_x,q_y)$ according to figure 3(d).

Figure 6 shows the same effects but for phase objects with distances d of 170 nm between irregularities of height s_0 of 100 nm. Again the double slit arrangement will be resolved even if the diffraction orders due to the grating structure are filtered out by the partial transfer function. In this case of a phase object the amplitudes of the resolved surface irregularities are much smaller than the original height difference of 100 nm.

Finally, figure 7 shows results for two horizontally shifted irregularities separated by distances $d = 170$ nm in (a) and (d), $d = 180$ nm in (b) and (e) and $d = 190$ nm in (c) and (f). Comparison of the subfigures corresponding to the same distance value d reveals that there is no difference in amplitude and phase resolution capabilities. Due to normalization, according to the generalized Rayleigh criterion two irregularities are resolved if the value of the local minimum at $x = 0$ is 0.735 [25]. This criterion holds for distances $d > 190$ nm. Thus, compared to conventional imaging the lateral resolution is improved by 36%. The situation corresponding to $d = 170$ nm leads to figures 5 and 6. Even in this case a local minimum is visible at $x = 0$.

A more general concept in this context treats the irregularities related to an object as point sources emitting spherical waves. With the point spread function (PSF) obtained from the MTF by an inverse 2D Fourier transform this leads to the Rayleigh resolution criterion for a conventional brightfield microscope. Even more, the lateral resolution of a conventional brightfield microscope can be improved by use of an annular aperture. As pointed out in a previous paper [20] this kind of resolution enhancement is closely related to the concept of partial transfer functions in interference microscopy. The normalized inverse 2D Fourier transform of a partial transfer function of rotational symmetry, i.e. $H_P(q_x,q_y) = H_P(q_\rho)$ leads to what we call a partial PSF:

$$h_P(\rho) = \frac{\int_0^\infty H_P(q_\rho)\,J_0(q_\rho\,\rho)\,q_\rho\,\mathrm{d}q_\rho}{\int_0^\infty H_P(q_\rho)\,q_\rho\,\mathrm{d}q_\rho} \qquad \text{with} \quad \rho = \sqrt{x^2+y^2}, \tag{20}$$

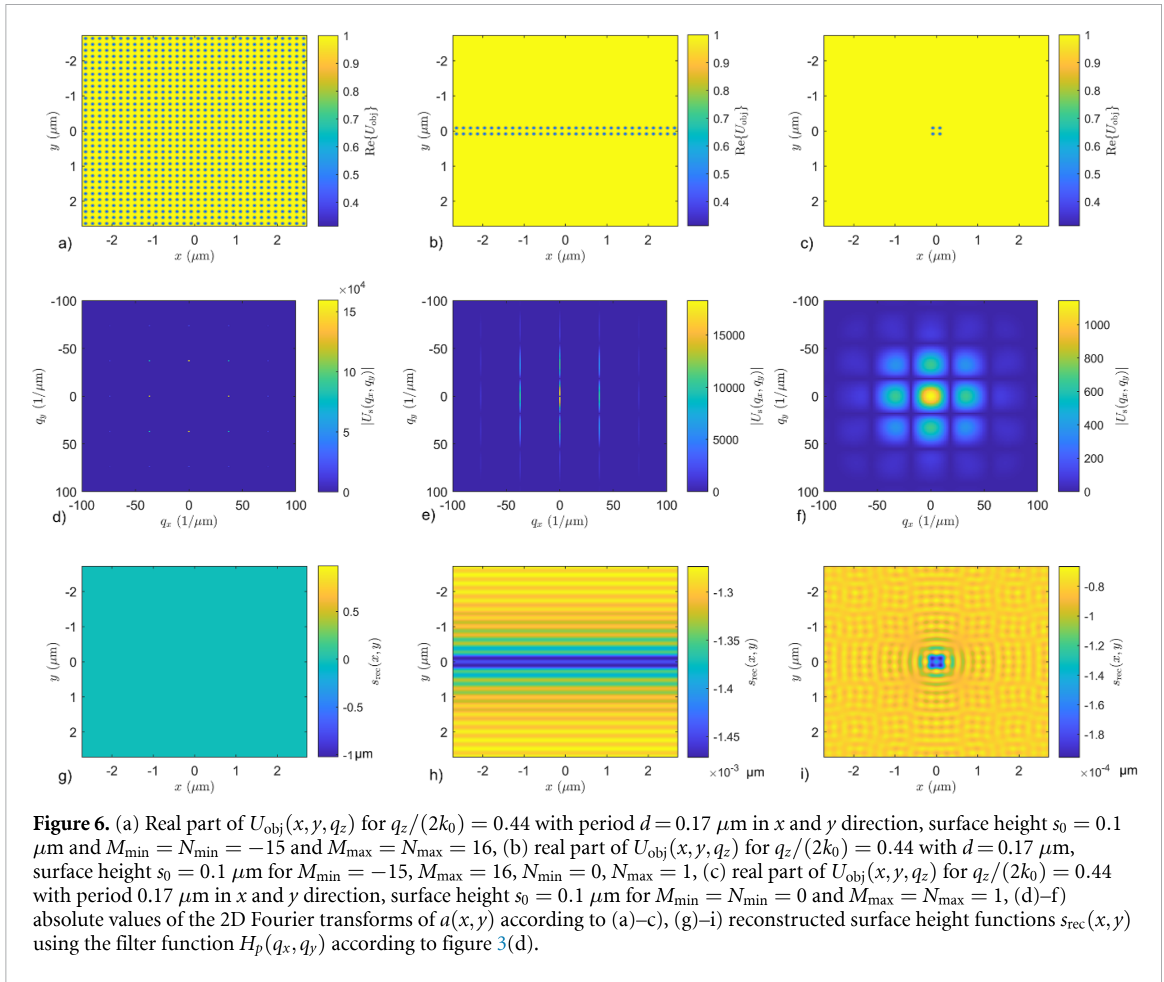

Figure 6. (a) Real part of $U_{obj}(x,y,q_z)$ for $q_z/(2k_0) = 0.44$ with period $d = 0.17$ μm in x and y direction, surface height $s_0 = 0.1$ μm and $M_{min} = N_{min} = -15$ and $M_{max} = N_{max} = 16$, (b) real part of $U_{obj}(x,y,q_z)$ for $q_z/(2k_0) = 0.44$ with $d = 0.17$ μm, surface height $s_0 = 0.1$ μm for $M_{min} = -15$, $M_{max} = 16$, $N_{min} = 0$, $N_{max} = 1$, (c) real part of $U_{obj}(x,y,q_z)$ for $q_z/(2k_0) = 0.44$ with period 0.17 μm in x and y direction, surface height $s_0 = 0.1$ μm for $M_{min} = N_{min} = 0$ and $M_{max} = N_{max} = 1$, (d)–(f) absolute values of the 2D Fourier transforms of $a(x,y)$ according to (a)–c), (g)–i) reconstructed surface height functions $s_{rec}(x,y)$ using the filter function $H_p(q_x,q_y)$ according to figure 3(d).

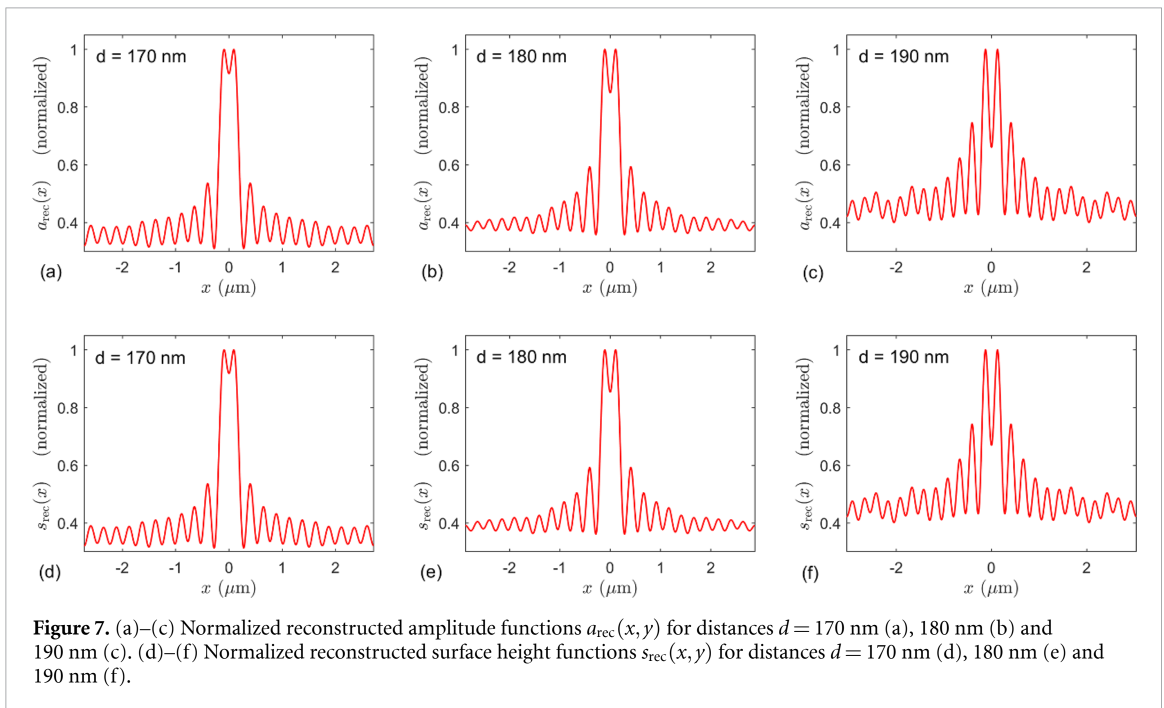

Figure 7. (a)–(c) Normalized reconstructed amplitude functions $a_{rec}(x,y)$ for distances $d = 170$ nm (a), 180 nm (b) and 190 nm (c). (d)–(f) Normalized reconstructed surface height functions $s_{rec}(x,y)$ for distances $d = 170$ nm (d), 180 nm (e) and 190 nm (f).

and $J_0(\ldots)$ the zero order Bessel function of the first kind. In order to achieve an optimum lateral resolution we take the partial transfer function at $q_z = q_{z,min}$. In figure 8(a) this partial PSF is compared to the Airy disc and the PSF for a narrow annular ring aperture of maximum diameter. Compared to the PSF for this annular

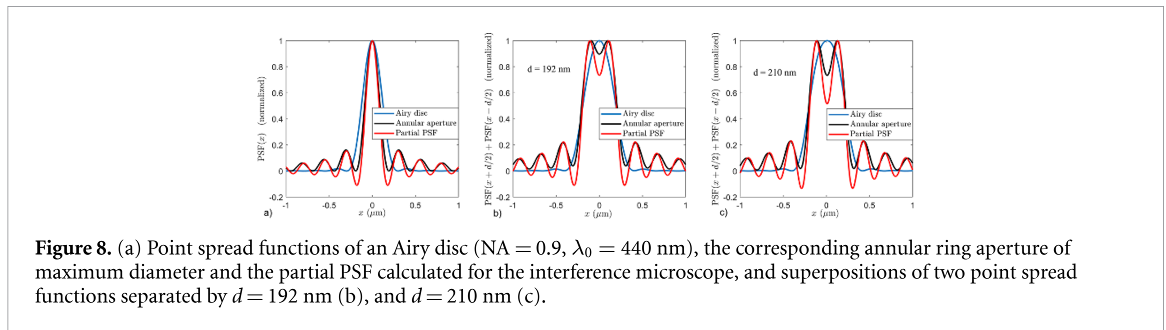

Figure 8. (a) Point spread functions of an Airy disc (NA = 0.9, $\lambda_0 = 440$ nm), the corresponding annular ring aperture of maximum diameter and the partial PSF calculated for the interference microscope, and superpositions of two point spread functions separated by $d = 192$ nm (b), and $d = 210$ nm (c).

aperture the partial PSF is slightly narrower, but shows stronger side lobes. This is due to the fact that the partial PSF directly corresponds to the inverse 2D Fourier transform of the partial transfer function, whereas the PSF of a brightfield microscope is related to intensity and thus to the absolute square of the inverse 2D Fourier transform of a circular ring. Figures 8(b) and (c) represent superpositions of two PSFs laterally separated by $d = 192$ nm (b) and 210 nm (c). For $d = 192$ nm the partial PSF $h_P(x)$ fulfills the generalized Rayleigh criterion, i.e. the value at $x = 0$ is 0.735 times the maximum value [25], whereas for the PSF of the annular aperture a distance $d = 210$ nm is needed in order to fulfill the Rayleigh criterion. Note that the Rayleigh resolution obtained from the Airy disc is 298 nm for an NA of 0.9 and a wavelength λ_0 of 440 nm. For comparison, the Sparrow criterion [12] leads to a lateral resolution of 164 nm for the partial PSF, 172 nm for the annular PSF, and 230 nm for the PSF given by the Airy disc.

4. Experimental results

Figure 9 shows results obtained with the self-build Linnik interferometer introduced in section 1 comprising two 100× objective lenses of NA= 0.9 and a royal blue LED ($\lambda_0 = 447$ nm, FWHM ≈ 20 nm) for illumination. The first object under investigation is a nanoscale linewidth/pitch standard fabricated by Supracon AG [41]. For certain linewidth/pitch values d the standard provides a rectangular grating (dark rectangles at the bottom of the subimages in figure 9) as well as two parallel bars separated by a distance d (top part of the calibration structure according to figure 9). Measurement results for $d = 230$ and $d = 200$ nm are shown in figure 9. The upper subfigures (a) and (b) display interference patterns occurring at the focus position. Subfigures (c) and (d) show reconstructed topographies obtained via phase analysis of the interference data of an image stack recorded during a depth scan. In both cases the double bar structure is resolved, whereas the grating structure is not. Profile sections taken from the topography data shown in subfigures (c) and (d) are plotted in subfigures (e) and (f), respectively. These results confirm the theoretical assumption according to which the two-point resolution is superior compared to the Abbe resolution limit for the corresponding grating. Note, that the experiments were conducted with a Linnik interferometer in a standard configuration. Only the evaluation wavelength for the lock-in phase calculation [42, 43] was specifically adapted to values of 700 nm in figures 9(c), (e) and 740 nm in figures 9(d) and (f).

Another experimental result is shown in figure 10. In this case, the sample was fabricated by a focused ion beam system. The individual structures consist of two craters 200 nm apart with a bar of less than 50 nm width in between. Figure 10(a) is a scanning electron microscope (SEM) image of a cluster of five double craters. Figures 10(b)–(d) represent results of interferometric phase analysis using an evaluation wavelength of 700 nm (b), 560 nm (c) and 790 nm (d). Height profiles corresponding to single columns of figures 10(c) and (d) are shown in subfigures (e) and (f). The profiles are separated by constant height offsets of 20 nm for better visibility. Although the double crater structure is not resolved at the evaluation wavelength of 560 nm, it can be clearly recognized at 700 and 790 nm evaluation wavelength. This confirms the concept of the different partial transfer functions, which depend on the evaluation wavelength as introduced in section 2. Note that the noise superimposing the reconstructed surface topography increases for longer evaluation wavelengths due to the reduced amplitude of the corresponding interference component.

The experimental results from both samples exhibit additional side lobes as predicted by the simulations introduced in section 3. The side lobes can be seen as ghost images of the double bar structure in figures 9(c) and (d) and as additional grooves surrounding the double crater structures in figures 10(b) and (d). The variation of the maximum height differences in figures 10(b)–(d) is a consequence of the lateral resolution improvement: The better the lateral resolution, i.e. the longer the evaluation wavelength, the closer the

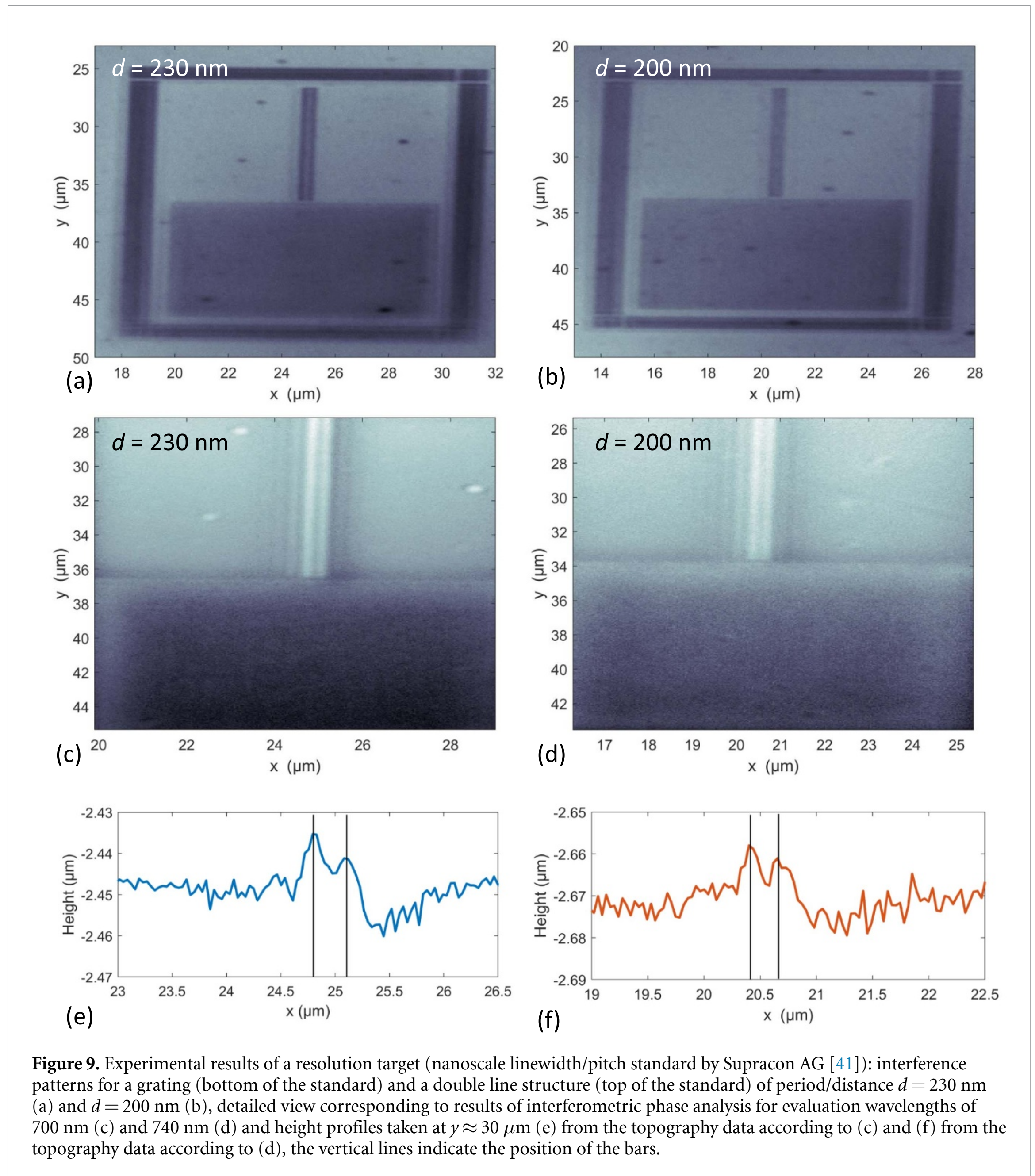

Figure 9. Experimental results of a resolution target (nanoscale linewidth/pitch standard by Supracon AG [41]): interference patterns for a grating (bottom of the standard) and a double line structure (top of the standard) of period/distance $d = 230$ nm (a) and $d = 200$ nm (b), detailed view corresponding to results of interferometric phase analysis for evaluation wavelengths of 700 nm (c) and 740 nm (d) and height profiles taken at $y \approx 30$ μm (e) from the topography data according to (c) and (f) from the topography data according to (d), the vertical lines indicate the position of the bars.

measured height values are to the real surface heights. This effect is already mentioned in earlier publications [23, 24]. However, the physical origin of the side lobes is due to the sharp transition at the edges of the partial transfer function. Consequently, reducing the sharp edges of the transfer function by an appropriate apodization filtering in the spatial frequency domain may reduce the side lobes without significantly affecting the lateral resolution capabilities.

The different evaluation wavelengths chosen in figures 9 and 10 elucidate the compromise between optimizing the lateral resolution and the signal-to-noise ratio of the interference signals. Note that the wavelength bandwidth of the light emitted by the blue LED is approximately 20 nm. Hence, the light is no longer monochromatic, what leads to a significant reduction of the values of $H(q_x, q_y, q_z)$ at higher transversal spatial frequencies q_x and q_z compared to the monochromatic case shown in figure 3 [21].

Although the experimental results obtained so far demonstrate the increase in resolution in a single lateral direction only, we expect that the resolution enhancement behaves isotropic, i.e. apart from aberrations of the optical system the lateral resolution enhancement is independent of the direction. This is due to the fact that the 3D TF shows rotational symmetry.

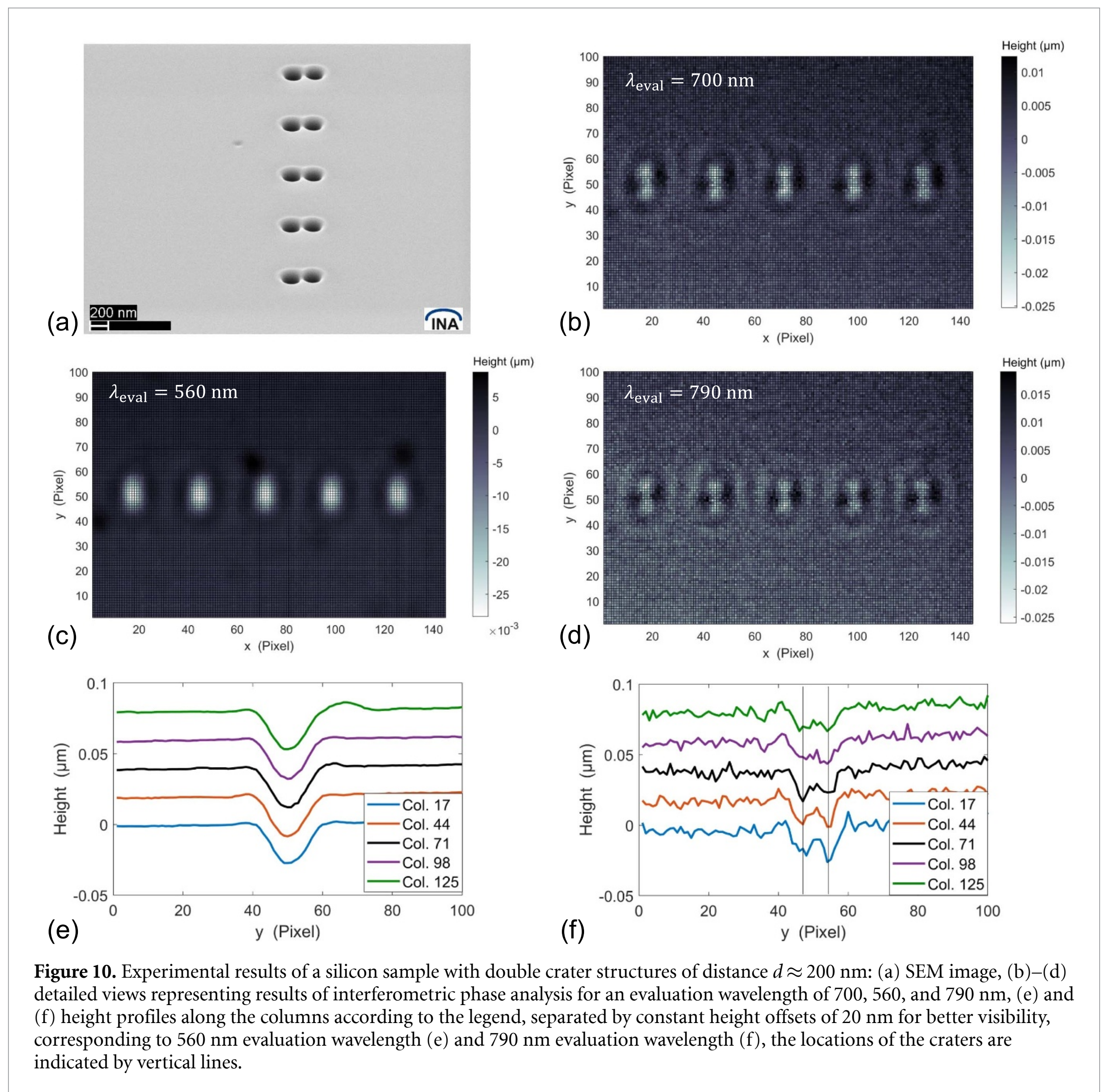

Figure 10. Experimental results of a silicon sample with double crater structures of distance $d \approx 200$ nm: (a) SEM image, (b)–(d) detailed views representing results of interferometric phase analysis for an evaluation wavelength of 700, 560, and 790 nm, (e) and (f) height profiles along the columns according to the legend, separated by constant height offsets of 20 nm for better visibility, corresponding to 560 nm evaluation wavelength (e) and 790 nm evaluation wavelength (f), the locations of the craters are indicated by vertical lines.

5. Conclusion

In this contribution the previously introduced three-dimensional transfer function of a CSI instrument is used to build a virtual interference microscope of high numerical aperture and to study its lateral resolution capabilities close to the resolution limit. Both, amplitude and phase objects are being examined. Furthermore, these objects are either optical gratings, two-point irregularities or combinations of both. Hence, the corresponding criteria characterizing the lateral resolution capabilities are either based on the fundamental Abbe limit or on the Rayleigh criterion, which holds for two irregularities separated by a certain distance. It turns out that for grating structures the Abbe limit represents a fundamental limitation even in interference microscopy. On the other hand, if two points on an object are to be resolved, interference microscopy provides a significantly superior lateral resolution compared to conventional microscopy. This is due to the 3D transfer characteristics of an interference microscope, where the lateral resolution capabilities depend on the axial spatial frequency value, which is closely related to the wavelength, at which an interference signal resulting from a so-called depth scan is analyzed. Furthermore, the electric field reflected from the object is the input quantity in interference microscopy instead of intensity in conventional microscopy and other types of optical microscopes. The highest lateral resolution is achieved for the longest evaluation wavelength. In this case the lateral resolution of an interference microscope is approximately 36% better than the lateral resolution defined according to the Rayleigh criterion in conventional microscopic imaging with spatially incoherent illumination. This is a consequence of the fact that long evaluation wavelengths are due to oblique angles of incidence. Thus, choosing a long evaluation wavelength in the signal analysis algorithm affects the lateral resolution in a similar manner as an annular aperture. At the lateral resolution limit the relevant partial transfer function of an interference microscope acts as a virtual annular

aperture, since only oblique light rays contribute to the object reconstruction from a stack of interferograms. The results presented here give an advanced understanding of the physical mechanisms of interference microscopy. They can be applied to both, phase as well as amplitude objects and demonstrate for the first time that the lateral resolution capabilities of an interference microscope surpass those of conventional brightfield microscopy.

Data availability statement

The data that support the findings of this study are available upon reasonable request from the authors.

Acknowledgments

The partial support of this work by the Deutsche Forschungsgemeinschaft (DFG, LE 992/13-3) is gratefully acknowledged.

ORCID iDs

Peter Lehmann https://orcid.org/0000-0003-0051-5066
Thomas Kusserow https://orcid.org/0000-0002-0567-3437

References

[1] Hell S W *et al* 2015 The 2015 super-resolution microscopy roadmap *J. Phys. D: Appl. Phys.* **48** 443001
[2] Cremer C and Masters B R 2013 Resolution enhancement techniques in microscopy *Eur. Phys. J.* H **38** 281–344
[3] Gustafsson M G L 2000 Surpassing the lateral resolution limit by a factor of two using structured illumination microscopy *J. Microsc.* **198** 82
[4] Darafsheh A 2022 Microsphere-assisted microscopy *J. Appl. Phys.* **131** 031102
[5] Wang F, Liu L, Yu P, Liu Z, Yu H, Wang Y and Li W J 2016 Three-dimensional super-resolution morphology by near-field assisted white-light interferometry *Sci. Rep.* **6** 24703
[6] Kassamakov I, Lecler S, Nolvi A, Leong-Hoï A, Montgomery P and Hæggström E 2017 3D super-resolution optical profiling using microsphere enhanced Mirau interferometry *Sci. Rep.* **7** 3683
[7] Hüser L and Lehmann P 2020 Microsphere assisted interferometry with high numerical apertures for 3D topography measurements *Appl. Opt.* **59** 1695–702
[8] Federici A and Dubois A 2015 Full-field optical coherence microscopy with optimized ultrahigh spatial resolution *Opt. Lett.* **40** 5347
[9] Mukhtar H, Montgomery P, Anstotz F, Barillon R and Rubin A 2018 Immersion white light scanning interferometry using elastic polymer path length compensation *SPIE Proc.* **10678** 1067816
[10] Born M and Wolf E 2013 *Principles of Optics: Electromagnetic Theory of Propagation, Interference and Diffraction of Light* (Amsterdam: Elsevier)
[11] Horikawa Y 1994 Resolution of annular-pupil optical systems *J. Opt. Soc. Am.* A **11** 1985–91
[12] H Gross (ed) 2005 *Handbook of Optical Systems* (*Physical Image Formation* (*W. Singer, M. Totzeck, H. Gross*)) vol 2 (New York: Wiley)
[13] D Malacara (ed) 2007 *Optical Shop Testing* (New York: Wiley)
[14] Sheppard C J R, Gu M, Kawata Y and Kawata S 1994 Three-dimensional transfer functions for high-aperture systems *J. Opt. Soc. Am.* A **11** 593–8
[15] Sheppard C, Connolly T and Gu M 1993 Imaging and reconstruction for rough surface scattering in the Kirchhoff approximation by confocal microscopy *J. Mod. Opt.* **40** 2407–21
[16] Sheppard C J R, Gu M and Mao X Q 1991 Three-dimensional coherent transfer function in a reflection-mode confocal scanning microscope *Opt. Commun.* **81** 281–4
[17] Coupland J and Lobera J 2008 Holography, tomography and 3D microscopy as linear filtering operations *Meas. Sci. Technol.* **19** 074012
[18] Su R, Coupland J, Sheppard C and Leach R 2021 Scattering and three-dimensional imaging in surface topography measuring interference microscopy *J. Opt. Soc. Am.* A **38** A27–A41
[19] Lehmann P, Künne M and Pahl T 2021 Analysis of interference microscopy in the spatial frequency domain *IOP J. Phys. Photonics* **3** 014006
[20] Lehmann P and Pahl T 2021 Three-dimensional transfer function of optical microscopes in reflection mode *J. Microsc.* **284** 1–11
[21] Lehmann P, Hagemeier S and Pahl T 2021 Three-dimensional transfer functions of interference microscopes *Metrology* **1** 122–41
[22] de Groot P and Colonna de Lega X 2020 Fourier optics modeling of interference microscopes *J. Opt. Soc. Am.* A **37** B1–B10
[23] Lehmann P, Xie W, Allendorf B and Tereschenko S 2018 Coherence scanning and phase imaging optical interference microscopy at the lateral resolution limit *Opt. Express* **26** 7376–89
[24] Lehmann P, Tereschenko S, Allendorf B, Hagemeier S and Hüser L 2019 Spectral composition of low-coherence interferograms at high numerical apertures *J. Eur. Opt. Soc.* **15** 5
[25] Sheppard C J R 2017 Resolution and super-resolution *Microsc. Res. Tech.* **80** 590–8
[26] Tolmon F R and Wood J G 1956 Fringe spacing in interference microscopes *J. Sci. Instrum.* **33** 236
[27] Creath K 1989 Calibration of numerical aperture effects in interferometric microscope objectives *Appl. Opt.* **28** 3333–8
[28] Biegen J 1989 Calibration requirements for Mirau and Linnik microscope interferometers *Appl. Opt.* **28** 1972–4
[29] Sheppard C and Larkin K 1995 Effect of numerical aperture on interference fringe spacing *Appl. Opt.* **34** 4731–4
[30] McCutchen C W 1964 Generalized aperture and the three-dimensional diffraction image *J. Opt. Soc. Am.* **54** 240–4

[31] de Groot P and Colonna de Lega X 2004 Signal modeling for low-coherence height-scanning interference microscopy *Appl. Opt.* **43** 4821–30

[32] Abdulhalim I 2001 Theory for double beam interferometric microscopes and experimental verification using the linnik microscope *J. Mod. Opt.* **48** 279–302

[33] Abdulhalim I 2006 Competence between spatial and temporal coherence in full field optical coherence tomography and interference microscopy *J. Opt. A: Pure Appl. Opt.* **8** 952–8

[34] Beckmann P and Spizzichino A 1987 *The Scattering of Electromagnetic Waves From Rough Surfaces* (Norwood, MA: Artech House, Inc.)

[35] Sheppard C 1998 Imaging of random surfaces and inverse scattering in the Kirchoff approximation *Waves Random Media* **8** 53–66

[36] Coupland J, Mandal R, Palodhi K and Leach R 2013 Coherence scanning interferometry: linear theory of surface measurement *Appl. Opt.* **52** 3662–70

[37] Goodman J W 2005 *Introduction to Fourier Optics* 3rd edn (Englewood, CO: Roberts and Company Publishers)

[38] Garces D H, Rhodes W T and Pena N M 2011 Projection-slice theorem: a compact notation *J. Opt. Soc. Am.* A **28** 766–9

[39] de Groot P and Colonna de Lega X C 2006 Interpreting interferometric height measurements using the instrument transfer function *Fringe 2005* (Berlin: Springer) pp 30–37

[40] de Groot P, Colonna de Lega X, Su R, Coupland J and Leach R 2021 Modeling of coherence scanning interferometry using classical Fourier optics *Opt. Eng.* **60** 104106

[41] Supracon A G 2022 Nanoscale Linewidth Pitch Standard (available at: www.supracon.com/en/nanoscale_linewidth_pitch_standard.html)

[42] Fleischer M, Windecker R and Tiziani H 2000 Fast algorithms for data reduction in modern optical three-dimensional profile measurement systems with MMX technology *Appl. Opt.* **39** 1290–7

[43] Tereschenko S 2018 Digitale Analyse periodischer und transienter Messsignale anhand von Beispielen aus der optischen Präzisionsmesstechnik *PhD thesis* University of Kassel